

Chapter 3

Ion-Implantation Induced Layer Transfer of Single Crystalline Barium Titanate Thin Films

3.1 Introduction

In this chapter, we examine the optimization of the ion implantation process by studying the layer transfer of barium titanate thin films onto silicon-based substrates. Hydrogen and helium ions were co-implanted to facilitate ion-implantation-induced layer transfer of films from barium titanate single crystals. From thermodynamic equilibrium calculations, we suggest that the dominant species during cavity nucleation and growth are H_2 , H^+ , H_2O , Ba^{2+} and Ba-OH , and that the addition of hydrogen to the Ba-Ti-O system can effectively suppress volatile oxide formation during layer transfer and subsequent annealing. After ion implantation, barium titanate layers contain microstructural defects and hydrogen precipitates in the lattice, but after layer transfer, the single crystal is found to be stoichiometric. Using direct wafer bonding and layer splitting, single crystal barium titanate thin films were transferred onto amorphous silicon nitride and Pt substrates. Micro-Raman spectroscopy indicated that the density of defects generated by ion implantation in barium titanate can be significantly reduced during post-transfer annealing, returning the transferred layer to its single crystal state. Characterization using piezoresponse force microscopy shows that the layer-transferred thin films are ferroelectric, with domain structures and piezoresponse characteristics similar to that of bulk crystals. ¹

3.2 Ferroelectric Materials

Ferroelectric materials have attracted increased attention as device materials in recent years because of their potential applications in microelectronics and integrated optics [105]. Furthermore, these

¹This chapter is based on work done with Dr. Young-Bae Park [87].

materials are attractive for microelectromechanical systems (MEMS) applications due to large displacement and high output force during actuation [93].

Many different methods have been studied to obtain high quality, thin film ferroelectric layers [125]. The growth of epitaxial thin films at relatively high temperatures ($> 700^{\circ}\text{C}$) has been reported using metal organic chemical vapor deposition, molecular beam epitaxy, atomic layer deposition, pulsed laser deposition, chemical solution deposition, and sol-gel processes. Integration of most of these technologies with conventional silicon-based device applications has proven difficult because of the high growth temperatures required and the need for an epitaxial template. Due to the complex set of elastic and electric boundary conditions at each grain, the grains in pressed ceramics and polycrystalline films are usually composed of multiple domains. If the spontaneous polarization within each domain is random, or distributed in such a way as to lead to zero net polarization, the pyroelectric and piezoelectric effects of individual domains will partially or significantly compensate each other. Additionally, for photonic devices, grain boundaries and domain boundaries can be sources of light scattering and absorption.

Recently, progress on integration of single crystal ferroelectrics has been made by fabrication of single crystal thin film layers. Light elements such as hydrogen and helium are implanted into a wafer at a specified projected range, and a film of equivalent thickness is exfoliated [22, 114]. Recently, successful layer transfer of semiconductors and ferroelectric materials has been reported [15, 54, 65, 74, 115, 127]. In the work reported here, layer transfer relies on direct wafer bonding and gas pressure-induced layer exfoliation. This is similar to that used to fabricate silicon-on-insulator structures, and enables much thinner films to be fabricated. We discuss hydrogen release and the resulting cavity growth mechanisms for the layer splitting of barium titanate (BaTiO_3), and the role of hydrogen during post-thermal annealing. Together with the thermodynamics and kinetics of cavity nucleation, growth, and blistering, these results provide an explanation of the layer exfoliation process. In this study, H^+ and He^+ were implanted in single crystal BaTiO_3 and subsequently bonded to silicon nitride $\text{Si}_3\text{N}_4/\text{Si}$ and Pt/Si receptor substrates, which are typical structures for ferroelectric memory and MEMS devices. Pt is typically used as a bottom electrode in ferroelectric capacitors and Si_3N_4 is typically used as an etch-stop layer in MEMS devices.

3.3 Experimental Work

Protons were implanted into single-crystal BaTiO₃ with energy between 20 and 80 keV with a dose of $5 \times 10^{16} - 1 \times 10^{17} \text{ cm}^{-2}$, followed by 30 - 115 keV He⁺ implantation with a dose of $1 \times 10^{17} \text{ cm}^{-2}$. All implantations were performed at room temperature. The donor and receptor substrates (sputtered Pt on Si and low-pressure chemical vapor deposition Si₃N₄ on Si) were cleaned with methanol, acetone, and deionized water. The donor and receptor substrates were brought in contact at room temperature. Heating during the initial bonding step causes micro-cracks to form and cavities to nucleate, coalesce, and blister in the implanted region. Isochronal annealing of the bonded donor material was performed between 300 and 500°C after initial bond formation, causing a layer whose thickness is equal to the implanted depth to be transferred to the receptor substrate.

The thermodynamic equilibrium composition at the annealing temperature (300 - 700°C) was calculated using the SOLGASMIX-PV code in Chemsage [5], minimizing the total Gibbs free energy of the system with data from the Joint-Army-Navy-Air Force (JANAF) thermochemical table [40]. Calculations were performed for both Ba-Ti-O and Ba-Ti-O-H systems with the compound conditions of 1:1:3 and 1:1:3:0.1-10, respectively, corresponding to stoichiometric single crystal BaTiO₃ with and without the addition of hydrogen.

Blistering was observed by polarized optical microscopy, scanning electron microscopy and atomic force microscopy. Atomic force microscopy was also used to characterize transferred film thickness and surface roughness. Micro-Raman spectroscopy, Rutherford backscattering spectroscopy, forward recoil elastic spectroscopy, energy dispersive x-ray spectroscopy, and transmission electron microscopy analyses were performed to assess the microstructural evaluation of the bulk crystal and transferred layer. Ferroelectric domain imaging and microscopic hysteresis loop measurements were obtained using piezoresponse force microscopy.

3.4 Analysis of the Layer Transfer Process

The key factors required to achieve covalent bonding between donor and receptor substrates are high surface flatness, low surface roughness, surface cleanliness, and chemical reactivity. Initial bonding of bulk, unimplanted BaTiO₃ crystals was successful since the donor and receptor substrates can be prepared according to these conditions. Bulk (100) BaTiO₃ has a typical lamellar domain pattern with tetragonal 90° a-axis and c-axis domains with sizes ranging from 5 to 400 nm, with a root-mean squared (RMS) roughness of 2.0 nm. Due to the alternating a-c tetragonal domain structure,

the surface of the BaTiO₃ sample is corrugated with a characteristic angle between domains given by: $\theta = 90^\circ - 2\arctan(a/c)$ where a and c refer to lattice constants of the [100] and [001] axes respectively. The peak-to-valley height of this surface corrugation was found to be in the range of 2 - 100 nm, depending on the domain size. The RMS roughness of the BaTiO₃ donor wafer slightly increased after ion implantation to 2.4 nm. Using a Monte Carlo simulation method for calculation of ion implantation and collision cascade characteristics [6], the ion projected range was determined to be ~ 430 nm [6]. The Pt coating thickness was 180 nm and the Si₃N₄ thickness was 50 nm, yielding a receptor substrate RMS roughness of 0.7 nm for Si₃N₄ coated Si substrates and 3.6 nm for Pt coated Si substrates. After room temperature bonding, no interference fringes were observed, indicating a distinct lack of surface particles or other contamination.

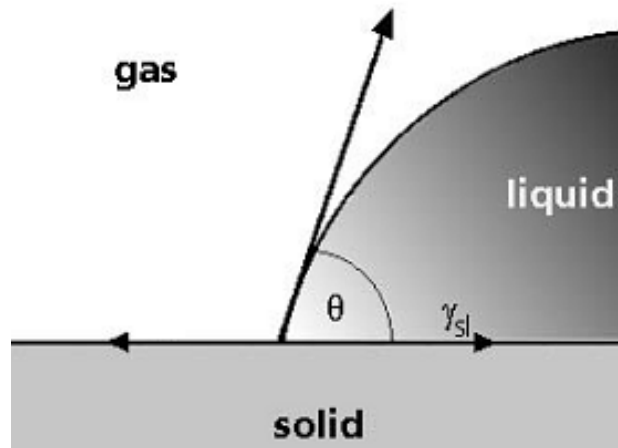


Figure 3.1. Typical solid-liquid-gas contact angle schematic.

The surface energy of the BaTiO₃ single crystals surfaces following H⁺ implantation was obtained by contact angle measurements using water and di-iodomethane droplets with a constant volume droplet of 20 dm³ using a double laser-beam goniometer. At room temperature, the surface energy is 61.1 mJ/m² and for the temperature-dependent surface energy, we used the phenomenological equation, $\gamma(T) = 6.11 \times 10^{-2} + 3.82 \times 10^{-5}T$ assuming $\gamma(T) = \gamma_0(1 + T/T_0)$, where T_0 is the critical temperature at which the solid-gas interface vanishes [46].

3.4.1 Hydrogen Behavior in Ba-Ti-O-H Phases

After ion implantation, the bulk BaTiO₃ lattice is filled with hydrogen. This hydrogen passivates the dangling bonds and defects generated by atomic displacements. In order to describe the behavior of hydrogen in solid materials, Sieverts law can be applied. Here: $c_0 = sp_e^{1/2}$ where pressure, p_e , is related to fugacity, f_e , and the hydrogen concentration, c_0 , in the solid at equilibrium [81]. The depth profile of implanted hydrogen is determined by post-implantation diffusion as well as the as-implanted projected range profile. During annealing the hydrogen concentration profile in the solid is assumed to be in local equilibrium with hydrogen gas filled cavities. Generation of a large internal gas pressure within the cavities occurs as the material achieves local equilibrium, and thus the hydrogen concentration can be related to the input fugacity of the source hydrogen and cavity inner pressure formed during annealing.

Phase equilibrium calculations for a system composed of Ba, Ti, O, and H were performed. For constant pressure and temperature conditions, the equilibrium state is defined by a global minimum in the Gibbs free energy. We searched for the global Gibbs free energy minimum by adjusting the proportions of chemical components across all of the possible species and phases as shown in Table 3.1, in which the 19 possible gaseous and 17 possible solid equilibrium and non-equilibrium species are shown for the Ba-Ti-O-H system. Phases that are thermodynamically unstable disappear in the search for the global Gibbs free energy minimum. We started the calculation with a fixed number of moles of Ba, Ti, O, and H, which were randomly distributed over the possible species. Phase equilibrium was defined by the values of the three independent variables that minimized the Gibbs free energy. This optimization problem was solved using SOLGASMIX-PV [5]. The independent variables were perturbed randomly to search for the global free energy minimum at fixed P and T conditions.

Figure 3.2 shows the phase diagrams with equilibrium solid-gas species varying with respect to annealing temperature. In the absence of hydrogen, solid BaTiO₃ along with volatile Ti and Ba oxides are predicted as shown in Figure 3.2(a). The different panels in (a) - (e) correspond to the calculation at different cavity pressures. The pressures are (a) 1.33×10^{-3} Pa without any implanted hydrogen, (b) 1.33×10^{-3} Pa after hydrogen implantation, (c) 1.33×10^3 Pa, (d) 6.7×10^6 Pa, and (e) 13.4×10^6 Pa. For the bulk BaTiO₃, we assumed that the crystal was in vacuum. On the other hand, for the system with hydrogen, we assumed that hydrogen resides at the ion projected range and forms micro-cavities during post-implantation processes. Figures 3.2(b) - (e) clearly

Table 3.1. Possible equilibrium species in the Ba-Ti-O-(H) chemistry obtained from JANAF thermochemical data and SOLGASMIX-PV code.

Gas Phase
$H_2, H^+, H_2O, HO^-, HO_2, H_2O_2, O^{2-}, O_2, O_3$
$Ba^{2+}, BaH^{3+}, BaOH^+, Ba_2, Ba(OH)_2, BaO, Ba_2O, (BaO)_2TiO, TiO_2, Ti^{4+}$
Solid Phase
$BaTiO_3, Ba_2TiO_4, BaO, BaH_2, Ba, Ba(OH)_2, BaO_2TiH_2, TiO(\alpha)$
$TiO(\beta), Ti_2O_3, TiO_2(\text{rutile}), TiO_2(\text{anatase}), Ti_3O_5, Ti_4O_7, Ti, H_2O, H_2O_2$

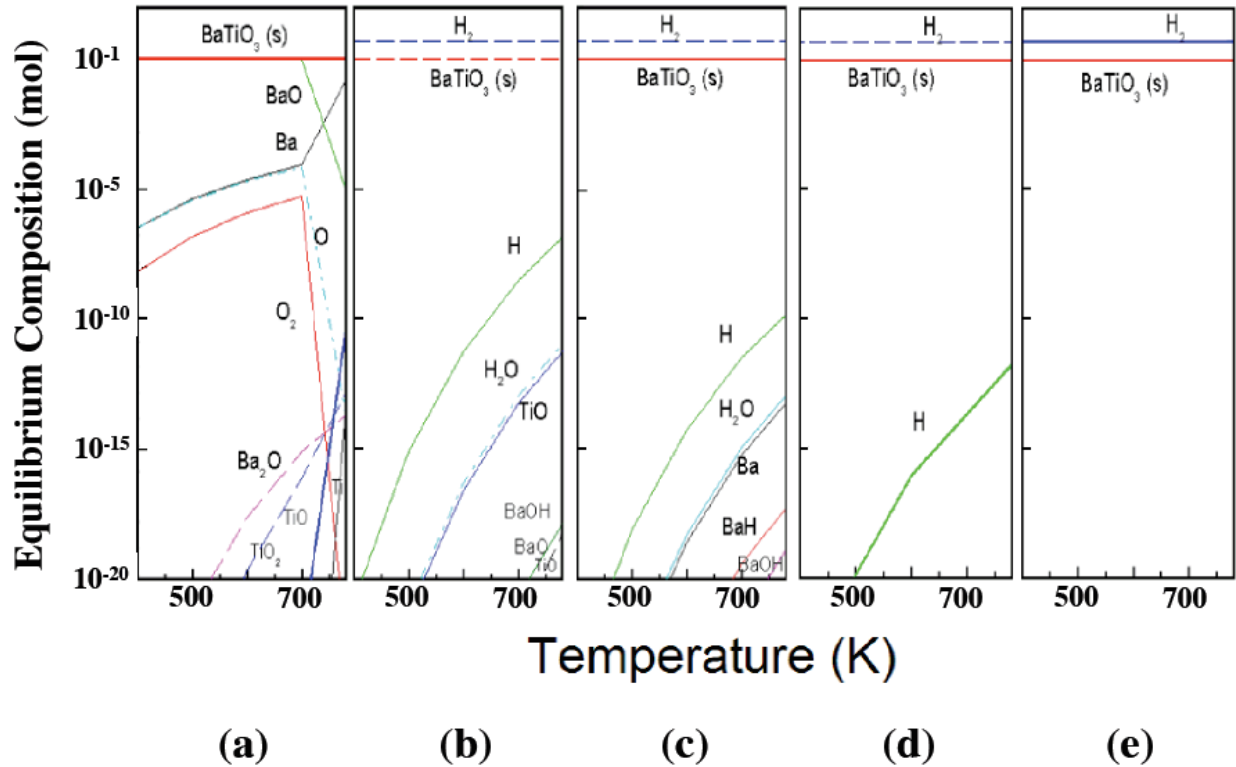


Figure 3.2. Equilibrium composition as a function of annealing temperature from 8×10^{-4} Pa - 1.33 MPa. The different panels in (a) - (e) correspond to the calculation at different cavity pressures. The pressures are (a) 1.33×10^{-3} Pa without any implanted hydrogen, (b) 1.33×10^{-3} Pa after hydrogen implantation, (c) 1.33×10^3 Pa, (d) 6.7×10^6 Pa, and (e) 13.4×10^6 Pa.

show a significant decrease, followed by disappearance of many of the volatile gas phase species, e.g. Ba^{2+} , Ba-O , Ba-OH , Ba-H , Ti^{4+} , and Ti-O with an increase of pressure. The calculations suggest that volatile oxide formation during high temperature annealing processes can cause the ratio of Ba^{2+} to Ti^{4+} to O^{2-} to become non-stoichiometric. However, in the presence of hydrogen, these oxide compounds can be effectively suppressed [Figure 3.2(b)]. The pressurized hydrogen reduces the formation of volatile oxides and acts as an agent for cavity nucleation, growth, and blistering during the layer transfer process.

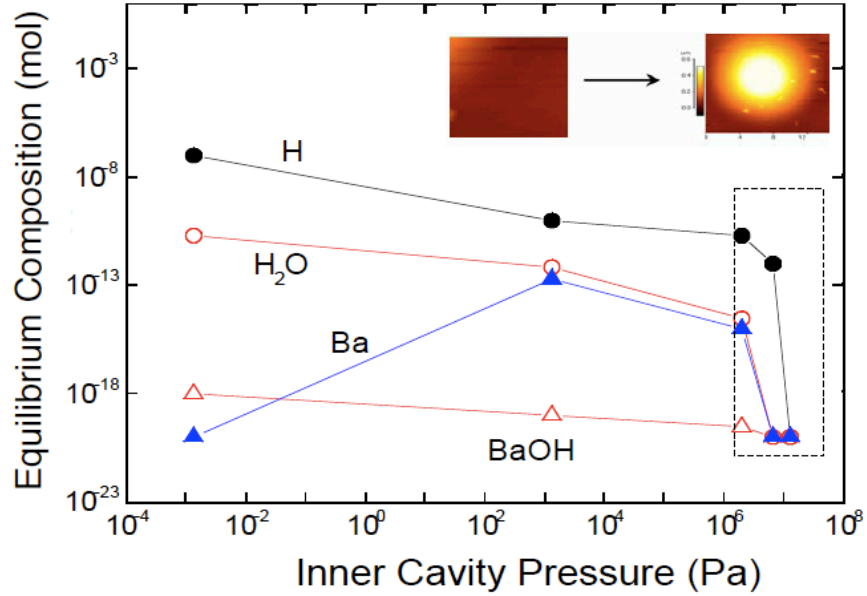


Figure 3.3. The change of pressure-dependent equilibrium composition in the Ba-Ti-O-H system at 500°C from Figure 3.2. The theoretically calculated cavity inner pressure from cavity geometry with radius and height measured by AFM ranges from 8×10^{-4} Pa to 0.2 GPa.

The change in concentration of gas species as a function of cavity inner pressure and geometry during annealing is shown in Figure 3.3. The inner pressure is calculated based on cavity dimensions measured from atomic force microscopy and assuming that cavity nucleation occurs uniformly in all directions in the plane of ion implantation. The excess pressure in the cavity relative to ambient pressure is written as:

$$\Delta p = \frac{64hEd^3}{12r^4(1-\nu^2)} \quad (3.1)$$

where E is the Young's modulus (120 GPa for BaTiO_3), d is the thickness of the layer, h is the height of the cavity, and ν is Poisson's ratio (0.3) [90]. The calculated cavity pressures were between 2 and 200 MPa. The main species in this pressure range ($> 10^{-9}$ mol) are H_2 , H^+ , H_2O , Ba^{2+} , and Ba-OH . In this range, there are no Ti-related species due to the lower free energy of formation of Ba-oxide species. In the range of pressures studied, the hydrogen gas partial pressure caused cavity nucleation followed by lateral cavity expansion. After the pressure reaches the point of cavity nucleation, the cavity begins to expand spontaneously in the rectangle area.

3.4.2 Cavity Formation and Real Hydrogen Behavior

During ion implantation, the implanted hydrogen atoms can combine with one of elements in the BaTiO_3 lattice forming X-H or X-OH complexes (where X is Ba or Ti) as shown by equilibrium calculations. During subsequent thermal annealing, implanted hydrogen diffuses in the vicinity of the implantation depth to form microcavities filled with H_2 . The high pressure inside a cavity acts as the driving force for its growth and expansion at the initial stage of annealing [115]. The minimum implanted hydrogen dose to enable blistering can be estimated to be:

$$\Phi_{min} = 8\gamma/3k_B T \quad (3.2)$$

where γ is a surface energy and k_B is Boltzmann's constant [43, 110]. Considering the surface energy of BaTiO_3 , one can estimate the minimum dose to be greater than 2×10^{15} ions/ cm^2 , which is consistent with reported values for other ferroelectric materials [96]. The ion dose used in this study ($> 1 \times 10^{16}$ cm^{-2}) was therefore high enough for cavity growth and blistering, Figure 3.4(a).

In order to investigate hydrogen diffusion during annealing, forward recoil electron scattering spectroscopy is used. This technique measures the depth at which hydrogen and deuterium are elastically scattered from an incident beam of energetic particles. In this case 2 MeV He^+ was used at the Cambridge Accelerator at Harvard University. Figure 3.5(a) shows the spectra for hydrogen in the implanted bulk BaTiO_3 after annealing at different temperatures where channel number 150 - 400 correspond to approximately 1 - 1.7 MeV for the energy of the recoiled particle. The behavior of hydrogen during the cavity growth and layer transfer process has been extensively studied in silicon [95, 121, 122]; however, no detailed reports on the hydrogen bonding configurations in the ferroelectric material systems have been reported. FT-IR studies in MIR geometries have revealed that the initial implantation damage, hydrogen passivation of internal defects and surfaces, and

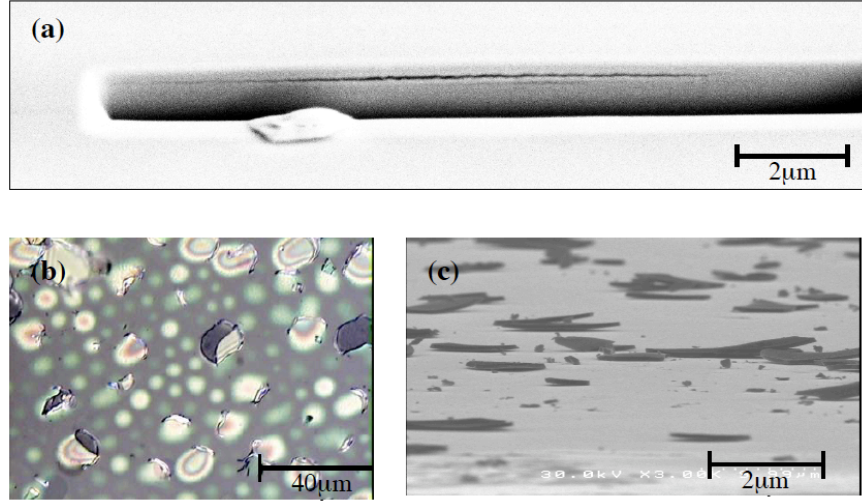


Figure 3.4. (a) FIB image of a cavity after Ga ion etching, (b) optical microscope image of cavity distribution and blistering, (c) SEM image of blisters on the sample surface. The average crater depth after the partial blistering is 450 nm for the lines and is consistent with the SRIM simulation results. The thickness is 450 - 500 nm as predicted by the SRIM simulation ($1 \times 10^{17} \text{ cm}^{-2}$, 80 keV).

the physical pressure created internally by H_2 formation are all essential elements for the layer splitting and exfoliation [12]. The desorption and out-diffusion of hydrogen with partial blistering are observed in the 300 - 500°C range. At 600°C, hydrogen concentration is comparable to surface contamination level and the overall surface of the BaTiO_3 was blistered, Figure 3.4(b) and (c).

In previous work, high concentrations of hydrogen have been shown to degrade the spontaneous polarization of ferroelectrics [15]. If hydrogen bonds to one of the elements in the lattice, polar hydroxyl $[\text{OH}^-]$ bonds can form and cause asymmetric stretching motion of the O-Ti-O bond. The change of symmetry in the Ti=O bond along the polarization axis of tetragonal unit cell would degrade the spontaneous polarization and actuating properties. However, in the Ba-Ti-O-H system, thermodynamic calculations of composition show that there are not a significant number of Ti-OH or Ti-H bonds, and considering the cavity inner pressure, there are no oxide species with high pressure hydrogen molecules. Also, Raman spectroscopy analysis shows no OH mode ($3200 \sim 3700 \text{ cm}^{-1}$, not shown here).

Forward recoil electron spectroscopy was also used to investigate the hydrogen desorption kinet-

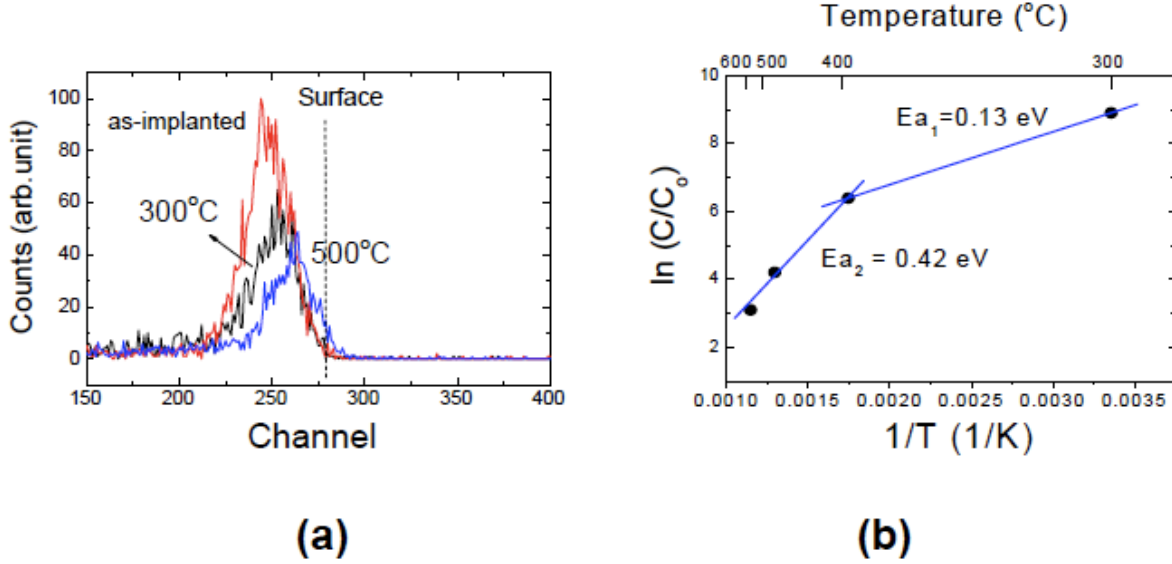


Figure 3.5. Forward recoil electron spectroscopy for (a) as-implanted BaTiO_3 ($1 \times 10^{17} \text{ cm}^{-2}$, 80 keV), annealed BaTiO_3 at 300°C and 500°C for 30 min. The He^+ beam (2 MeV) is incident at the angle of 150° relative to the sample surface. (b) Arrhenius-type reaction of hydrogen release from FRES count integration. The FRES peak is normalized by the initial concentration (C_0) of as-implanted sample with the H^+ dose of $1 \times 10^{17} \text{ cm}^{-2}$ at 80 keV.

ics. By integrating the spectroscopy measurements as a function of temperature, an Arrhenius-type reaction of hydrogen release was plotted, Figure 3.5(b). By measuring the slope of this plot, the activation energy for hydrogen release was experimentally determined to be ~ 0.42 eV. This is similar to the corresponding energies reported for silicon [15]. It is believed that the hydrogen release reaction is not only thermally activated but also induced by physical reaction pathways generated from implantation damage. Above 600°C , there is no considerable amount of hydrogen detected in the bulk BaTiO_3 .

Upon thermal release of hydrogen throughout the implanted layer, the hydrogen will diffuse to form small cavities. As the pressure in these cavities increases with time, cracks begin to form and beyond a critical radius, it will be energetically favorable for the cracks to continue growing until they merge with other cavities throughout the film. The final result is a fully exfoliated layer of BaTiO_3 whose thickness corresponds to the peak depth of ion implantation. This process is discussed in detail by Han et al. [46]

3.4.3 Microstructure of Ion Damaged Barium Titanate

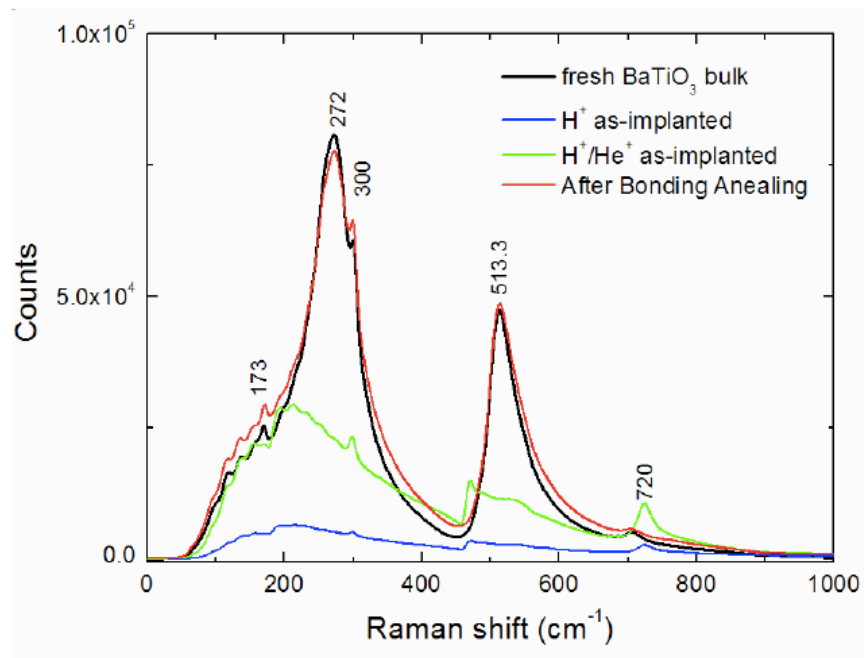


Figure 3.6. Micro-Raman spectra for the BaTiO₃ sample before processing, after the two implantation steps, and after bonding and annealing. The final spectra matches that of the sample before processing, indicating that proper post-bond annealing can return the transferred layer to its original, single crystal state.

In Figure 3.6, micro-Raman spectroscopy shows an unprocessed, bulk BaTiO₃ sample with a small shoulder peak at 305 cm⁻¹ and a broader peak at 710 cm⁻¹ [101]. These peaks are assigned to tetragonal BaTiO₃ and vanish above the Curie temperature. The two broad bands centered at 272 and 513 cm⁻¹ correspond to transverse optical phonons and their widths can be explained by large anharmonic coupling and a frequency dependent damping constant. The 272 and 513 cm⁻¹ peaks are observed in both the cubic and tetragonal phases, although they are broader in the cubic phase. After high energy ion implantation, the bulk BaTiO₃ contains a damaged layer at the implantation depth. This corresponds to the low Raman active mode in the H⁺ and H⁺/He⁺ as-implanted curves. Before the final annealing step, the broad peak at 200 - 400 cm⁻¹, along with the absence of a sharp 305 cm⁻¹ peak and a broad 705 cm⁻¹ suggests that the BaTiO₃ in this

layer is significantly damaged due to large number of local defects, as well as large residual stresses. In previous work, the authors showed that the layer splitting mechanism induced a change in the hardness and Young's modulus of the implanted BaTiO₃ donor wafer [89]. This can be explained by an increase in strain near the bubble region during the layer exfoliation process. After post-bond annealing, the micro-Raman curve is almost identical to the unprocessed, single crystal BaTiO₃. The sharp peaks at 272, 300, and 513.3 cm⁻¹ are again present, and the smaller peak at 705 cm⁻¹ has dissipated. These results verify that proper post-bond annealing can return the transferred BaTiO₃ layer to its single crystal state.

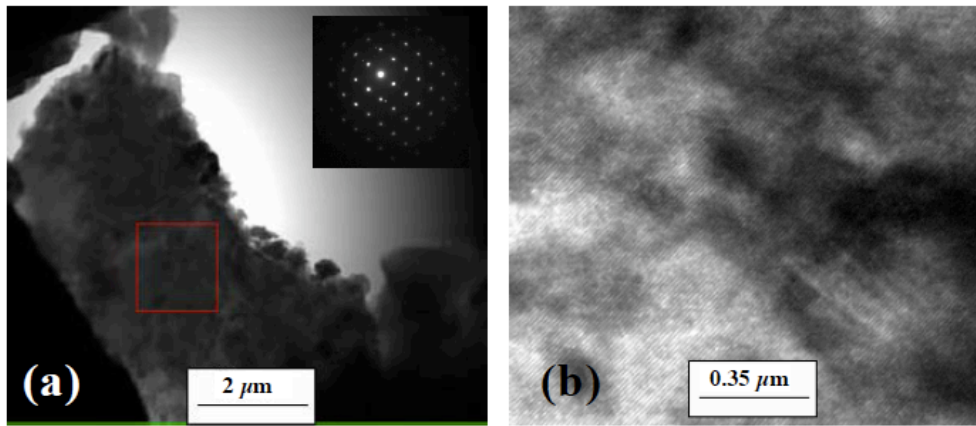


Figure 3.7. TEM images of layer transferred BaTiO₃. (a) shows a low magnification image with a selected area diffraction pattern along the (112) zone axis shown as an insert, and (b) shows a high resolution image of the film.

Figure 3.7 shows transmission electron microscope images of BaTiO₃ bonded to an amorphous carbon coated Cu grid. High resolution images, Figure 3.7(b), show that the BaTiO₃ film has a single-crystal lattice structure with a tetragonal lattice. This is confirmed by the selected area diffraction pattern shown as an inset in Figure 3.7(a). Energy dispersive x-ray spectroscopy scans confirm that the BaTiO₃ thin film has a stoichiometric Ba:Ti:O ratio of 1:1:3. These results show that the composition of the transferred BaTiO₃ film is the same as the donor wafer, and the crystallinity of this layer can be recovered after bonding and subsequent annealing.

3.4.4 Domain Characterization of the Transferred Ferroelectric Layer

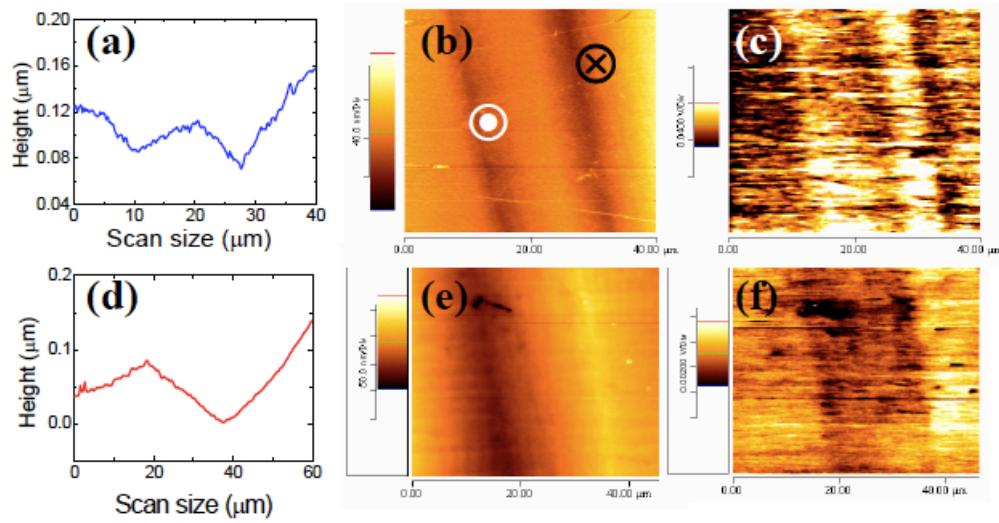


Figure 3.8. Comparison of surface morphology and polarization for bulk and transferred BaTiO₃. (a) AFM image of the transferred BaTiO₃ film, (b) PFM image of the transferred BaTiO₃ film, (c) AFM image of the bulk BaTiO₃, (d) PFM image of the bulk BaTiO₃, (e) AFM line scan of the transferred BaTiO₃ film along the domain walls, and (f) AFM line scan of the bulk BaTiO₃ film along the domain walls.

Single crystal barium titanate thin films with thicknesses between 150 and 800 nm were successfully transferred to Si₃N₄/Si and Pt/Si₃N₄/Si substrates. The 800 nm thick films on Pt/Si₃N₄/Si substrates were approximately 1 mm x 2 mm, and 400 nm thick films on Si₃N₄/Si were approximately 5 mm x 5 mm [89]. Atomic force microscopy line scans, Figure 3.8(a), of the transferred BaTiO₃ samples show a domain structure similar to that of bulk BaTiO₃, Figure 3.8(d). The c-domain (where the c-axis is oriented perpendicular to the film, Figure 2.2) and a-domain spacing in the transferred layer is approximately half of the equivalent distance in the bulk single crystal. This can be attributed to additional stresses which are imparted on the film during the layer transfer process. Piezoresponse force microscopy imaging in Figure 3.8(b) also shows c-a domain configurations similar to a bulk single crystal, Figure 3.8(e). The surface corrugation angle

($\theta = 90^\circ - 2\arctan(a/c)$) is $0.5 - 0.6^\circ$. In the piezoresponse image [Figure 3.8(c) and (f)], the bright and dark areas originate from regions where the polarization vectors point into and out of the plane, respectively. Since the domain structure is similar in both the single crystal and the transferred layer, one can conclude that layer transfer yields high-quality films with properties very similar to bulk single crystals.

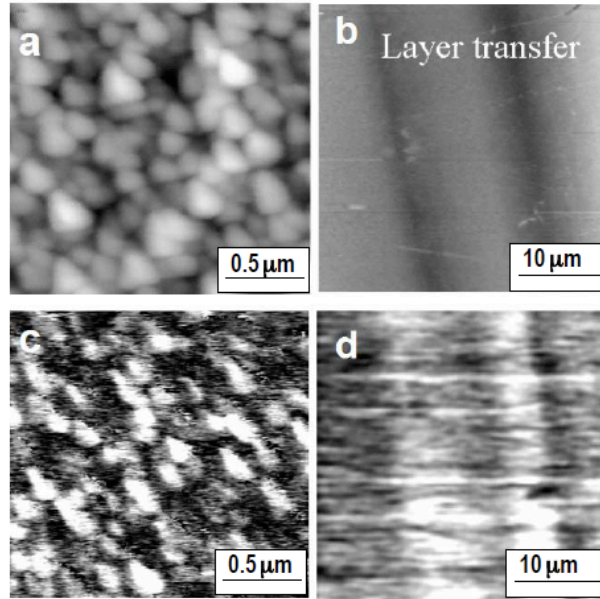


Figure 3.9. Comparison of AFM [(a) and (b)] and PFM [(c) and (d)] images for the BaTiO₃ thin films. (a) and (c) are of a PLD BaTiO₃ thin film. (b) and (d) are of a layer transferred thin film BaTiO₃. PFM measurement conditions were $V_{ac} = 1.5$ V and a tip frequency of 20 kHz. Note that the AFM/PFM images of both films show different lateral scan sizes.

For comparison, a BaTiO₃ film grown using pulsed laser deposition is shown in Figure 3.9(c) and (d). These films on Pt substrates produce crystallographically textured films which exhibit some grain misorientation. Their domain polarization characteristics and structure are influenced by domain misorientations and grain boundaries, Figure 3.9(d). Therefore, pulse laser deposited BaTiO₃ films exhibit grain scale morphology as opposed to the domain scale morphology of the transferred films.

In order to confirm the piezoelectric nature of the BaTiO₃ film, we obtained a hysteresis curve,

Figure 3.10, for a single ferroelectric domain. Here the conducting atomic force microscope tip served as the top electrode. While both BaTiO₃ films showed piezoelectric hysteresis, the transferred film showed a larger piezoresponse, larger effective piezoelectric constant (d_{33}^{eff}) of 90 pm/V, and smaller coercive field (~ 20 kV/cm) than the donor substrate. Clamping effects are taken into account using the equation:

$$d_{33}^{eff} = d_{33} - \frac{2d_{31}s_{13}}{s_{11} + s_{12}} \quad (3.3)$$

The resulting single crystal d_{33} value, $d_{33} = 129$ pm/V, is consistent with those reported elsewhere [59, 87, 102, 103].

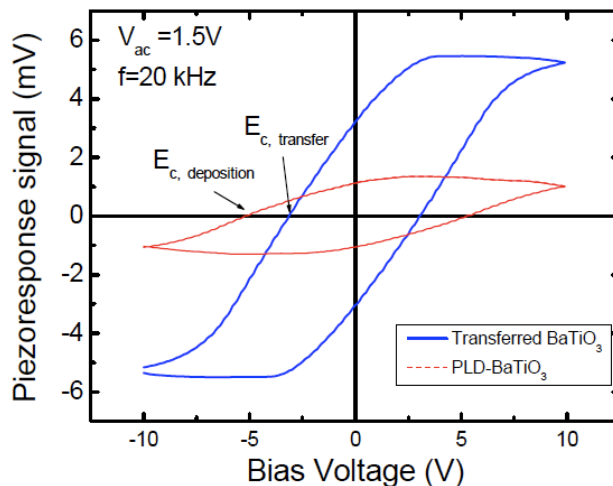


Figure 3.10. Local piezoresponse hysteresis curves comparing PLD BaTiO₃ on a Pt/Si substrate and layer transferred BaTiO₃ on Pt.

3.5 Conclusion

In this chapter we have performed single-crystal layer transfer and have reported mechanisms for cavity formation in ion-implanted, single-crystal BaTiO₃. Analysis of the equilibrium concentration of species as a function of annealing temperature was performed. From this, it was shown that released hydrogen during thermal annealing suppresses the formation of volatile oxides which might otherwise degrade the performance of the ferroelectric films. The hydrogen pressure inside the

platelets created during thermal annealing was sufficiently high to form cavities inside the implanted substrate. BaTiO₃ films, 150 - 800 nm thick, have been transferred onto Pt and Si₃N₄ layers. Micro-Raman analysis showed that lattice damage to the BaTiO₃ that occurs during the layer transfer process can be effectively removed with proper annealing. The transferred BaTiO₃ thin films show domains identical to those found in bulk crystals. Piezoresponse force microscopy shows that the film is piezoelectrically active with domain configurations similar to that of bulk crystals. The transferred films show larger piezoresponse and smaller coercive fields than those associated with BaTiO₃ films grown by traditional methods. Based on these results, ion implantation-induced layer transfer has been successfully utilized to create high-quality single-crystal ferroelectric thin films that can be bonded to substrates with significant thermal expansion mismatch.